Numerical simulation of carrier collection and recombination at grain boundaries in $Cu(In, Ga)Se_2$ solar cells

K. Taretto, and U. Rau

Citation: Journal of Applied Physics **103**, 094523 (2008);
View online: https://doi.org/10.1063/1.2917293
View Table of Contents: http://aip.scitation.org/toc/jap/103/9
Published by the American Institute of Physics

Numerical simulation of carrier collection and recombination at grain boundaries in $Cu(In,Ga)Se_2$ solar cells

K. Taretto[1] and U. Rau[2,a)]
[1]*Departamento de Electrotecnia, Universidad Nacional del Comahue, Buenos Aires 1400, 8300 Neuquén, Argentina*
[2]*IEF5-Photovoltaik, Forschungszentrum Jülich, 52425 Juelich, Germany*

(Received 8 February 2008; accepted 2 March 2008; published online 14 May 2008)

Two-dimensional numerical device simulations investigate the influence of grain boundaries (GBs) on the performance of $Cu(In,Ga)Se_2$ solar cells. We find that the electronic activity of grain boundaries can reduce the efficiency of $Cu(In,Ga)Se_2$ solar cells from 20% to below 12% making proper passivation of GBs a primary requirement for high efficiency. Cell efficiencies larger than 19% require GB defect densities below 10^{11} cm^{-2}. Also, an internal band offset in the valence band due to a Cu-poor region adjacent to the GBs could effectively passivate grain boundaries that are otherwise very recombination active. It is shown that such a barrier must be more than 300 meV high and at least 3 nm wide to virtually suppress all grain boundary recombination. Contrariwise, such a barrier represents an obstacle for hole transport reducing carrier collection across grain boundaries that are not perpendicular to the cell surface. We further find that inverted grain boundaries lead to an accumulation of the short circuit current along the grain boundary, which in certain situations enhances the total short circuit current. However, we do not find any beneficial effect of any type of grain boundaries on the overall cell efficiency. © *2008 American Institute of Physics*. [DOI: 10.1063/1.2917293]

I. INTRODUCTION

$Cu(In,Ga)Se_2$ (CIGS) solar cells provide the highest power conversion efficiency of all thin-film photovoltaic devices.[1] The grain size g of these polycrystalline absorber films hardly exceeds the film thickness d of typically $d=1.5-2.5$ μm. The electronic activity of grain boundaries (GBs) in such a situation could be much more critical than in multicrystalline Si solar cells with g being of the order of $g=5-10$ mm. Interestingly, solar cells made from polycrystalline $CuInSe_2$ and CIGS absorbers reach efficiencies above 14% and 19% respectively,[1,2] markedly outperforming their 12.5% efficient monocrystalline counterparts.[3] This situation is very similar to that of polycrystalline CdTe solar cells but very different to that of multicrystalline/monocrystalline Si solar cells. During the past few years, considerable research effort was directed to understanding why the polycrystalline materials CdTe (Refs. 4 and 5) and CIGS (Refs. 6–17) yield such excellent photovoltaic absorbers. Especially, the question was discussed whether, and if yes, how GBs can be *beneficial* for CIGS and CdTe solar cells whereas they are detrimental for most other photovoltaic materials. In addition, there are several models that explain the low electronic activity of GBs in CIGS with the help of arguments concerning beneficial crystallography of GBs,[12] extrinsic defect chemistry based on the beneficial effect of oxygen[18,19] and sodium,[20,21] as well as a self-passivation effect by an internal valence band offset.[13,14]

The present work uses two-dimensional numerical simulations of polycrystalline CIGS solar cells to investigate the influence of GBs on their electrical performance. The results presented here extend earlier simulations[22,24] and incorporate analytical assessments of specific recombination and transport effects that may occur in polycrystalline CIGS. Concentrating on the question whether and under which circumstances CIGS cells may reach high efficiencies, the present simulations focus on the influence on solar cell performance of GB defect densities, bulk and GB defect energy and capture cross sections, grain sizes, and GB position (perpendicular and parallel to the cell surface). In order to obtain GB barrier heights of 100 meV consistent with experimental data,[6–9,12] our model requires a GB defect density of $N_{it} \approx 2\times10^{12}$ cm^{-2}. In such a situation, 19% efficiency cells are obtained only with a low GB electron capture cross section $\sigma_{it,n}=10^{-18}$ cm^2. Defects above midgap are shown to enhance the cell's short circuit current at defect densities above 2×10^{12} cm^{-2}, which ensure carrier population inversion around the GB. Additionally, we explore the possibilities for a polycrystalline semiconductor to outperform a single crystalline material in terms of photovoltaic performance. Our results show that this situation cannot be constructed by introducing GB defects into an absorber with excellent photovoltaic properties. Nevertheless, redistribution of a fixed amount of defects from the grain interior toward the GBs can be beneficial. Also, when starting with a relatively poor absorber bulk material, we find that additional GB defects may enhance at least the short circuit current.

It has been proposed that GBs in CIGS feature a hole barrier due to a Cu-poor layer surrounding the GB,[13,15] which would strongly reduce GB recombination. Here, we obtain an analytical expression that models the recombination rate at such a barrier by assuming different GB capture cross sections $\sigma_{it,n}$ and $\sigma_{it,p}$ for electrons and holes. In cells where the GB is perpendicular to the cell surface, the simu-

a)Author to whom correspondence should be addressed. Electronic mail: u.rau@fz-juelich.de.

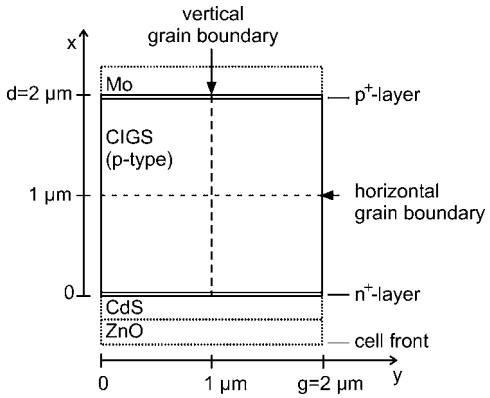

FIG. 1. Solar cell geometry considered in the simulations, with a cell thickness $d=2$ μm and a grain size $g=2$ μm, with a vertical GB at the coordinate $y=1$ μm (used in Secs. III and IV) or a horizontal GB (Sec. V). At the front of the cell, a ZnO top contact is followed by a CdS layer which forms a junction with the CIGS absorber. Our model mimics this junction using a 50 nm thick n^+-type CIGS layer placed at $x=0$. The Mo back contact and its corresponding $MoSe_2$ layer (not shown) are modeled by a 50 nm thick p^+-CIGS layer. The dotted layers are included in the calculations of the optical generation rate only.

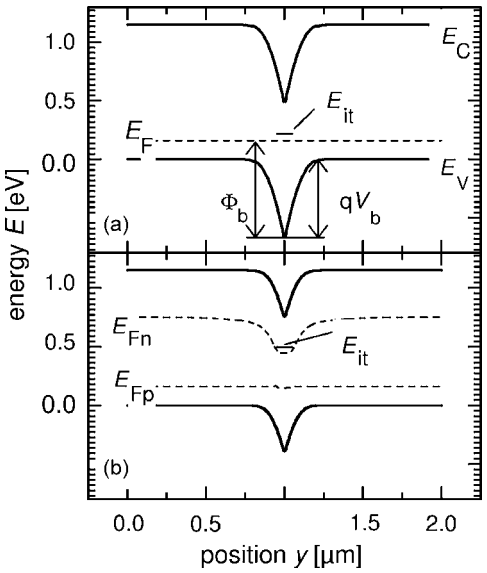

FIG. 2. Calculated band diagram in a CIGS solar cell under thermodynamic equilibrium (a) and during illumination under short circuit conditions (b), across a grain boundary (GB) located at $y=1$ μm (see Fig. 1). The energies E_V and E_C are the energies of the valence and conduction band edge, respectively, and E_{it} is the interface defect energy, here located at 0.880 eV above the valence band edge. Additionally shown are the GB barrier height Φ_b and the band-bending energy qV_b. In part b, the hole and electron quasi-Fermi levels E_{Fp} and E_{Fn}, are defined. The assumed GB trap density is $N_{it}=4\times10^{12}$ cm^{-2}.

lations show that a significant improvement of the efficiency requires an internal valence band offset $\Delta E_V = kT\log(\sigma_{it,n}/\sigma_{it,p}) > 300$ meV, where kT denotes the thermal energy. Up until this point, our results are consistent with earlier work.[22–24] Here, we also show that the width of the region with lowered valence band energy must be larger than 3 nm, otherwise quantum-mechanical tunneling reduces the passivation effect. If the GB is parallel to the cell surface, the high barriers represent an obstacle for hole transport that strongly reduce the device efficiency.

This paper is organized as follows: In Sec. II, we introduce the model, detailing the geometry, parameters, and solving method utilized for the simulations. Section III presents the simulation results for the case of a vertical grain boundary, followed by the analysis of the effects of the GB hole barrier in Sec. IV. Finally, Sec. V presents the simulations for horizontal GBs and in Sec. VI, we summarize and discuss the results.

II. MODEL

Figure 1 displays the assumed geometry of the ZnO/CdS/CIGS solar cell structure. For the computations discussed in Secs. III and IV, we assume a vertical GB placed along the center of the absorber yielding a columnar grain with a grain width of $g=2$ μm. Section III C adds results with a fourfold smaller grain size of $g=0.5$ μm. In Sec. V, we assume a horizontal GB dividing the absorber into two equal parts, as shown by the dashed line in Fig. 1. The CIGS absorber of thickness $d=2$ μm has a band gap energy $E_g=1.15$ eV. The photogeneration profile $G(x)$ is calculated from a coherent optical model[25] for the complete (300 nm)ZnO/(50 nm)CdS/(2 μm)CIGS/Mo stack illuminated with a 100 mW/cm^2 AM1.5G spectrum.[26] The generation profile inserted in our simulations corresponds to the absorption in the CIGS layer. The injection of carriers photogenerated in the CdS layer into the CIGS layer is incorporated by adding 30% of the CdS absorption[27] into the CIGS generation rate profile at coordinate $x=0$, i.e., at the CdS/CIGS interface. The integral of the resulting $G(x)$ profile yields a maximum available short circuit current density $J_{SC}^{max}=33.5$ mA/cm^2.

If not explicitly stated otherwise, we use the following material and device parameters: effective densities of states $N_C=10^{18}$ cm^{-3} and $N_V=10^{19}$ cm^{-3} for the conduction and valence bands, acceptor density $N_A=2\times10^{16}$ cm^{-3}, mobilities $\mu_p=10$ cm^2 V s^{-1} for holes and $\mu_n=100$ cm^2 V s^{-1} for electrons, and relative dielectric constant $\varepsilon=10$. We have assumed zero recombination at the CdS/CIGS interface as well as at the Mo back contact.

The electronic activity of GBs is modeled by defects situated at energies $E_{it}-E_V=270$, 605, or 880 meV, where E_V denotes the energy of the valence band maximum. One-half of the defects are assumed to be donorlike, the other half acceptorlike such that, in the limit of a high interface defect concentration N_{it}, the Fermi energy E_F is pinned at E_{it}. A pinning position at $E_{it}-E_V=270$ meV would lead to a band bending of about 100 meV at the GB that is compatible with the available experimental data[6–9,12] on CIGS, $E_{it}-E_V=880$ meV leads to type inversion at the grain boundary if N_{it} is sufficiently high, whereas $E_{it}-E_V=605$ meV corresponds to a trap level at the intrinsic Fermi energy E_i, i.e., a worst case scenario at equal capture cross sections for electrons and holes for the GB defects. Specific parameters that are used for the calculations presented in Figs. 2–8, 10, 11, 13, and 14 are summarized in Table I.

The simulation of the electronic transport is carried out for the CIGS part of the device only, by solving the stationary Poisson equation, and the current continuity equations combining drift and diffusion currents.[28] In the continuity

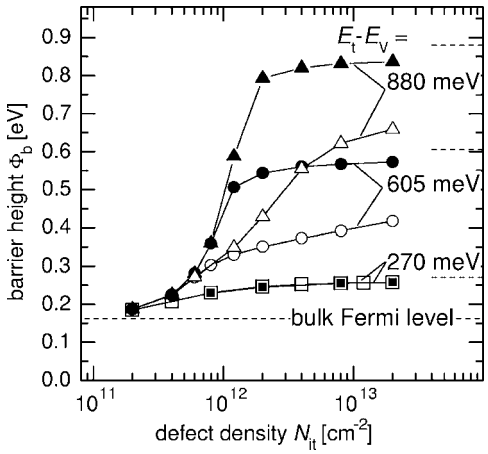

FIG. 3. Grain boundary barrier heights Φ_b with increasing GB defect density N_{it} calculated in CIGS solar cells at a depth of $x=1$ μm (see Fig. 2) under illuminated, short circuit conditions (open symbols), and in the dark (full symbols). Shallow defect levels (squares) located at $E_{it}-E_V=270$ meV above the valence band edge yield small barrier heights that are only weakly increased by the addition of defect levels, and are unaffected by illumination. Defects at $E_{it}-E_V=605$ meV (circles) and $E_{it}-E_V=880$ meV (triangles) build up significant GB barriers with increasing density N_{it}, saturating at $N_{it}=4\times10^{12}$ cm^{-2} in the dark due to Fermi level pinning. These high barriers are drastically reduced by illumination (open circles, open triangles).

equations, we insert the difference between the photogeneration profile $G(x)$ and the local net recombination rate, calculated as the sum of radiative and nonradiative defect-level recombination. The net radiative recombination rate is locally evaluated using the expression

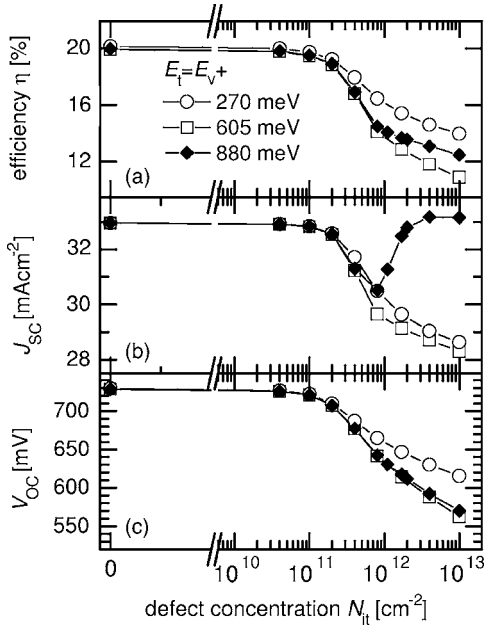

FIG. 4. Calculated efficiency η, short circuit current density J_{SC}, and open circuit voltage V_{OC} for a CIGS solar cell with grain size $g=2$ μm. The doping concentration is $N_A=2\times10^{16}$ cm^{-3} and the bulk defect concentration is $N_{bt}=2\times10^{15}$ cm^{-3}. Bulk as well as GB defect levels use equal electron and hole capture cross sections $\sigma_{bt,n/p}=\sigma_{it,n/p}=10^{-15}$ cm^2 and energy levels at 270/605/880 meV (squares, circles, diamonds) above the valence band edge.

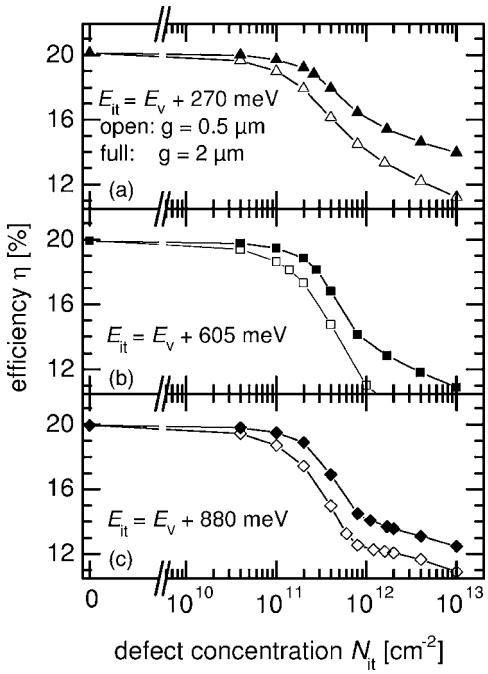

FIG. 5. Simulated dependence of cell efficiency η on the defect concentration N_{it} for grain sizes $g=0.5$ μm (open symbols) and 2 μm (full symbols), and GB trap energies 270 meV (a), 605 meV (b), and 880 meV (c) above the valence band edge. With the assumed capture cross sections of $\sigma_{bt,n/p}=\sigma_{it,n/p}=10^{-15}$ cm^{-2}, efficiencies over 19% are reached by cells with defect concentrations below $N_{it}=2\times10^{11}$ cm^{-2} ($g=2$ μm) or $N_{it}=10^{11}$ cm^{-2} ($g=0.5$ μm).

$$R_{rad}=B_{rad}(np-n_i^2), \tag{1}$$

where we assume $B_{rad}=6\times10^{-11}$ cm^3 s^{-1}, according to optical characterizations in CIGS thin films,[29] n and p are local electron and hole concentrations, respectively, and n_i is the intrinsic carrier concentration. The bulk defect occupancy and recombination rate are evaluated using Shockley–Read–Hall (SRH) statistics at the assumed monoenergetic donor/

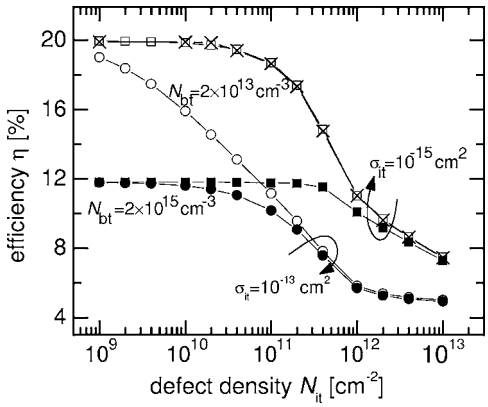

FIG. 6. Simulated dependence of cell efficiency η on the defect concentration N_{it} for grain sizes $g=0.5$ μm for bulk materials with defect concentrations $N_{bt}=2\times10^{15}$ cm^{-3} (open symbols) and $N_{bt}=2\times10^{13}$ cm^{-3} (full symbols) and a capture cross section $\sigma_{bt,n/p}=10^{-13}$ cm^2. The cell efficiencies decrease with increasing N_{it} to levels that depend on the assumed capture cross sections $\sigma_{it}=\sigma_{it,n/p}=10^{-15}$ cm^2 (full and open squares) and $\sigma_{it}=10^{-13}$ cm^2 (full and open circles) at the GBs. The data for a deeper bulk defect $E_{bt}-E_V=605$ meV (crosses) with $N_{bt}=2\times10^{15}$ cm^{-3} and $\sigma_{bt,n/p}=10^{-15}$ cm^2 [cf. Fig. 5(b)] show no difference to the data obtained for shallower bulk defects $E_{bt}-E_V=350$ meV (open squares).

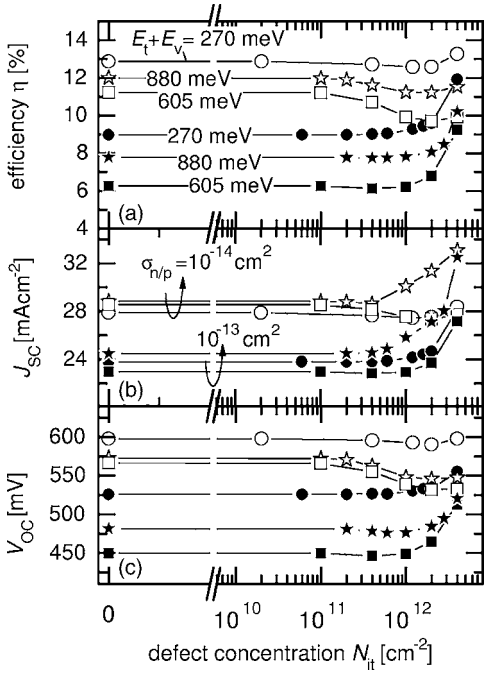

FIG. 7. Efficiency η, short circuit current density J_{SC}, and open circuit voltage V_{OC} for an average defect density $N_m=2\times10^{16}$ cm^{-3}. The increase in the concentration N_{it} of interface defects implies a reduction of the concentration N_{bt} of bulk defects following $N_{bt}=N_m-N_{it}/g$. Open symbols correspond to data with capture cross sections $\sigma_{bt,n/p}=\sigma_{it,n/p}=10^{-14}$ cm^2 while closed symbols use $\sigma_{bt,n/p}=\sigma_{it,n/p}=10^{-13}$ cm^2.

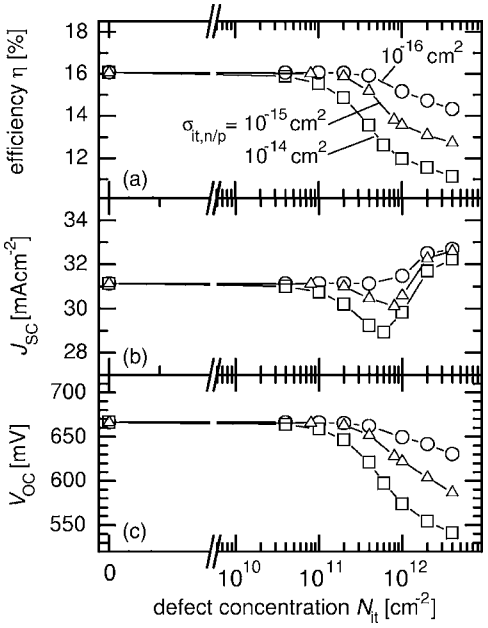

FIG. 8. Simulated efficiency η, short circuit current density J_{SC}, and open circuit voltage V_{OC} as a function of the concentration N_{it} of GB defects with energy $E_{it}=E_V+880$ meV and capture cross sections $\sigma_{it,p/n}=10^{-14}/10^{-15}/10^{-16}$ cm^2 (squares, triangles, circles). The bulk traps are placed at 605 meV above valence band edge, and have a density $N_{bt}=2\times10^{15}$ cm^{-3} and capture cross sections $\sigma_{bt,p/n}=10^{-14}$ cm^2.

acceptor defect level[30] with a concentration N_{bt}. The grain boundary is modeled as a true internal surface, where we specify the charge density,

$$Q_{it}=\frac{qN_{it}}{2}(1-2f_{it}), \tag{2}$$

per unit area, where q denotes the elementary charge and f_{it} the occupation function of the assumed donor/acceptor GB, as established by SRH statistics, which also yield the GB surface recombination rate

$$R_{it}=\frac{N_{it}v_{th}(n_{it}p_{it}-n_i^2)}{\sigma_{it,p}^{-1}(n_{it}+n_{1,it})+\sigma_{it,n}^{-1}(p_{it}+p_{1,it})}, \tag{3}$$

where v_{th} is the carrier thermal velocity, N_{it} is the GB defect density per unit area (i.e., the sum of acceptor and donor states), n_{it}, p_{it} are the local electron and hole concentrations at a given point of the GB line, and

$$n_{1,it}=N_C\exp\left(\frac{E_{it}-E_C}{kT}\right), \tag{4}$$

and

TABLE I. Defect energies E_{bt}, defect concentrations N_{bt}, and capture cross sections σ_{bt} for the bulk defects as well as the corresponding quantities E_{it}, N_{it}, and σ_{it} for the interface defects as used in the computations for Figs. 2–9, 11, 12, and 14. The sign "–" between two numbers indicates a covered range of the corresponding variable.

Figure	g (μm)	$E_{bt}-E_V$ (meV)	N_{bt} (cm^{-3})	σ_{bt} (cm^2)	$E_{it}-E_V$ (meV)	N_{it} (cm^{-2})	σ_{it} (cm^2)
2	2.0	880	2×10^{15}	10^{-15}	880	4×10^{12}	10^{-15}
3	2.0	270, 605, 880	2×10^{15}	10^{-15}	270, 605, 880	2×10^{11}–2×10^{13}	10^{-15}
4	2.0	270, 605, 880	2×10^{15}	10^{-15}	270, 605, 880	0–10^{13}	10^{-15}
5	2.0/0.5	270, 605, 880	2×10^{15}	10^{-15}	270, 605, 880	0–10^{13}	10^{-15}
6	0.5	350, 605	2×10^{13}, 2×10^{15}	10^{-13}	605	10^9–10^{13}	10^{13}, 10^{15}
7	2.0	270, 605, 880	(0–2)$\times10^{16}$	10^{-13}, 10^{-14}	270, 605, 880	(0–4)$\times10^{12}$	10^{-13}, 10^{-14}
8	2.0	605	2×10^{15}	10^{-14}	880	(0–4)$\times10^{12}$	10^{-16}–10^{-14}
9	2.0	605	2×10^{15}	10^{-14}	880	8×10^{10}–4×10^{12}	10^{-15}
11	2.0	270, 605, 880	2×10^{15}	10^{-15}	270, 605, 880	4×10^{12}	Electrons: 10^{-15} Holes: 10^{-21}–10^{-15}
12	2.0	270	2×10^{15}	10^{-15}	270	4×10^{11}, 4×10^{12}	Electrons: 10^{-15} Holes: 10^{-21}–10^{-15}
14	2.0	270	2×10^{15}	10^{-15}	270	4×10^{11}, 4×10^{12}	Electrons: 10^{-15} Holes: 10^{-21}–10^{-15}

$$p_{1,\mathrm{it}} = N_V \exp\left(\frac{E_V - E_{\mathrm{it}}}{kT}\right), \tag{5}$$

are auxiliary quantities.[30]

The two drift-diffusion equations together with the Poisson equation are simultaneously solved with a finite-element method using the software FEMLAB,[31] which is set to solve all equations simultaneously. An iterative Newton scheme for highly nonlinear problems is run on a strongly irregularly spaced finite-element mesh consisting of about 5000 s-order rectangular elements. On the front and back surfaces, we use mixed boundary conditions. Majority carriers are set to a fixed concentration given by the equilibrium value, while for minority carriers we impose a zero-flux condition, i.e., zero surface recombination. The electrostatic potential is set to zero at the front surface, and at the back surface to the sum of the applied voltage and the internal built-in voltage that results from calculating the electrostatics in thermal equilibrium. The mesh spacing immediately around the GB is typically 2.5 nm, while the minimum mesh spacing is 0.05 nm in the front space-charge region.

III. VERTICAL GRAIN BOUNDARIES

A. Grain boundary barrier heights and type inversion

For the electronic activity of GBs, we have to consider two different effects: first the areal charge density Q_{it} accumulated at the GB defects as given by Eq. (2) induces a band bending in the bulk neighboring the GB interface. Figure 2(a) shows a calculated band diagram under equilibrium conditions where the Fermi energy E_F at the GB is pinned to the energy E_{it} of the interface defects resulting in a band bending qV_b. The second consequence of GB defects results from their recombination activity. Under illumination, the quasi-Fermi levels E_{Fn} and E_{Fp} for electrons and holes are split, as shown in Fig. 2(b). The nonequilibrium charge carriers recombine following Eq. (3). In Eq. (3), the recombination current is not only proportional to the defect density N_{it} but it depends via Eqs. (4) and (5) on the defect energy E_{it}. Additionally, the band bending induced by the defect charge Q_{it} influences the free carrier concentrations n, p, and, consequently, also the recombination current. According to Eq. (3), a situation where $n=p$ is the most uncomfortable one at equal capture cross sections.

Figure 3 shows calculated barrier heights Φ_b across the GB, as defined in Fig. 2(a). For these calculations, we have assumed defects with capture cross sections $\sigma_{n/p} = 10^{-15}$ cm^2 and energies $E_{\mathrm{it}} = E_V + 270$, 605, and 880 meV with densities ranging from $N_{\mathrm{it}} = 2\times10^{11}$ to 2×10^{13} cm^{-2}. In addition to the doping density $N_A = 2\times10^{16}$ cm^{-3}, we consider a bulk defect density of $N_{\mathrm{bt}} = 2\times10^{15}$ cm^{-3} that limits the lifetime of the minority carriers in the bulk of the material. Under equilibrium conditions (full symbols, in Fig. 3) and with low interface defect density ($N_{\mathrm{it}} = 2\times10^{11}$), the barrier height Φ_b virtually equals the energy distance $E_F - E_C \approx 160$ meV in the bulk for all defect energies E_{it}, i.e., there is no energy barrier at the GB interface. Within the range from $N_{\mathrm{it}} = 8\times10^{11}$ to 4×10^{12} cm^{-2}, the barrier heights asymptotically approach the value of the corresponding defect energy (dashed lines in Fig. 3). For the interface defects close to the conduction band ($E_{\mathrm{it}} - E_V = 880$ meV), we therefore find type inversion when $N_{\mathrm{it}} \geq 8\times10^{11}$ cm^{-2}. The band diagram shown in Fig. 2(a) corresponds to such a situation under equilibrium conditions. Figure 2(b) shows the same configuration under illumination and demonstrates that the capture of minority carriers into the interface states significantly reduces Q_{it} and, consequently, the band bending around the GB.

The reduction of band bending and that of the GB barrier Φ_b by illumination is demonstrated more quantitatively by the open symbols in Fig. 3 especially for the trap energies $E_{\mathrm{it}} - E_V = 880/605$ meV whereas the curve with $E_{\mathrm{it}} - E_V = 270$ meV is barely affected by illumination. This latter situation appears to be the most probable in current CIGS cells, since, assuming a Fermi energy 160 meV above valence band edge, $E_{\mathrm{it}} - E_V = 270$ meV would yield a barrier of $qV_b = 110$ meV, in accordance with the available experimental data.[6–9,12]

B. Recombination via grain boundaries

Next, we turn to the consequences of GBs on the calculated photovoltaic output parameters. Figure 4 shows the efficiency η, short circuit current density J_{SC}, and open circuit voltage V_{OC} as a function of the GB defect density N_{it} in a CIGS solar cell with grain size $g = 2$ μm. The base of these calculations is CIGS with a concentration N_{bt} of bulk defects $N_{\mathrm{bt}} = 2\times10^{15}$ cm^{-3} and capture cross sections $\sigma_{\mathrm{bt},n/p} = 10^{-15}$ cm^2 corresponding to a bulk minority carrier lifetime of 5×10^{-8} s and a diffusion length $L_D = 3.6$ μm. Consequently, the photovoltaic performance of the reference computation for an interface trap density $N_{\mathrm{it}} = 0$ yields a high efficiency $\eta \approx 20\%$. The influence of GBs is now modeled by increasing the density of GB defects with capture cross sections $\sigma_{\mathrm{it},n/p} = 10^{-15}$ cm^2 at three different energies $E_{\mathrm{it}} = E_V + 270$, 605, and 880 meV. The device efficiency decreases by increasing the number of GB defects, independently of the energy position of the traps, obeying an augmented recombination of carriers. Although this is the expected overall consequence of increasing N_{it}, an exceptional trend takes place for the photocurrent density [Fig. 4(b)] in cells with traps at the energy $E_{\mathrm{it}} = E_V + 880$ meV, where J_{SC} is recovered beyond a minimum at $N_{\mathrm{it}} \approx 8\times10^{11}$ cm^{-2}. Our calculations reveal that the reincrease in J_{SC} toward the maximum available value at higher GB defect densities corresponds to the onset of type inversion at the GB under illumination. In this situation, the number of available holes limits GB recombination, and an increase in band bending at the GB reduces the recombination probability of electrons and, as a consequence, increases their collection probability.

However, the open circuit voltages V_{OC} displayed in Fig. 4(c) unveil that this specific improvement is restricted to the short circuit situation whereas under open circuit, recombination monotonically increases with increasing defect densities for *all* defect energies. This fact also dominates the overall performance shown in Fig. 4(a), demonstrating that the introduction of GB defects into a high quality CIGS absorber

material leads to a uniform decline of the efficiency η regardless of the assumed GB defect energy E_{it}.

C. Influence of grain size

Efficiencies in excess of 19% for CIGS solar cells are possible with grain sizes of only $g \approx 0.5$ μm, as shown in Ref. 2. In order to investigate the possibilities for such a high performance at such low grain sizes, we simulate cells with a vertical GB and a grain width $g=0.5$ μm, for different trap energies and increasing defect densities. Figure 5 shows the efficiency depending on N_{it} for $g=0.5$ μm (open symbols), and, for comparison, we include the results for $g=2$ μm (full symbols) extracted from Fig. 4(a). The bulk and GB defect energy is varied from $E_{it}-E_V=E_{bt}-E_V=270$ meV [Fig. 5(a)], to 605 meV [Fig. 5(b)], and 880 meV [Fig. 5(c)].

As expected, the smaller grain size yields lower efficiencies, regardless of the trap position. More importantly, our model indicates that efficiencies of $\eta=19\%$ require a very low defect density $N_{it}=10^{11}$ cm^{-2} for $g=0.5$ μm, whereas $N_{it}=2\times10^{11}$ cm^{-2} is needed for the larger grains ($g=2$ μm). In these cases, the corresponding band bendings are around $qV_b=25$ meV (cf. Fig. 3). We note here that $\eta \geq 19\%$ are also possible when using $N_{it}=4\times10^{12}$ cm^{-2} combined with electron capture cross sections $\sigma_{it,n}=10^{-18}$ cm^{-2}, i.e., much smaller than $\sigma_{it,n/p}=10^{-15}$ cm^{-2} used in Fig. 5. In this case (not shown), the band bending amounts to $qV_b=100$ meV.

D. Spatial distribution of defects

Up until this point, our calculations started with a rather perfect bulk material such that the efficiency level of the solar cells without GBs was higher than the record efficiencies.[1] Section III D investigates the interplay between bulk and GB defects. Figure 6 compares the influence of GB defects on the efficiency of solar cells having a high bulk minority carrier lifetime $\tau_b=(v_{th}N_{bt}\sigma_{bt})^{-1}=5\times10^{-8}$ s to the efficiency of cells with low $\tau_b=5\times10^{-10}$ s. We show here the example with a defect energy $E_{it}-E_V=605$ meV for the GB and $E_{bt}-E_V=350$ meV for the bulk defects. Variations of τ_b are achieved by the choice of $N_{bt}=2\times10^{15}$ cm^{-3} (open symbols) and $N_{bt}=2\times10^{13}$ cm^{-3} (full symbols) with a constant capture cross section $\sigma_{bt,n/p}=10^{-13}$ cm^2. The different choices of N_{bt} defines rather different efficiency levels of 20% and 11.8% at low values of $N_{it} \leq 2\times10^9$ cm^{-2}. However, the increase in N_{it} leads to a deterioration of the cell efficiencies that depends very much on the assumed capture cross sections $\sigma_{it,n/p}=10^{-15}$ cm^2 (squares) and $\sigma_{it,n/p}=10^{-13}$ cm^2 (circles) at the GBs. At high defect densities $N_{it} \geq 10^{12}$ cm^{-2}, the efficiencies are entirely determined by the GBs. Thus, Fig. 6 illustrates the transition between the extreme situations of a solar cell that is dominated by defects in the grain interior and a cell that is defined by its GB properties. In addition, Fig. 6 shows calculations for a deeper bulk defect $E_{bt}-E_V=605$ meV (crosses) with $N_{bt}=2\times10^{15}$ cm^{-3} and $\sigma_{bt,n/p}=10^{-15}$ cm^2 [i.e., data already shown in Fig. 5(b)]. We conclude from the comparison of these data with the results for $E_{bt}-E_V=350$ meV (open squares, $N_{bt}=2\times10^{13}$ cm^{-3} and $\sigma_{bt}=10^{-13}$ cm^2) that the choice of the bulk defect energy is rather irrelevant as long as the lifetime τ_b is high.

In our next numerical experiment, we investigate the influence of the spatial distribution of defects on the photovoltaic output parameters, by simulating cells with defects rather homogeneously distributed in the bulk to cells where the defects are concentrated at the coordinate of the vertical GB. These simulations assume cells where the bulk and the GB defect level have equal capture cross sections and energy level, gradually increasing N_{it} and reducing N_{bt}, thus maintaining the mean defect density N_m according to

$$N_m = N_{bt} + N_{it}/g. \tag{6}$$

The case of $N_{it}=0$ represents a monocrystalline material were all defects are homogeneously distributed in the bulk, whereas $N_{it}=4\times10^{12}$ cm^{-2} corresponds to the polycrystalline material where all defects are located at the GB. Figure 7 shows the photovoltaic output parameters as a function of N_{it} using $N_m=2\times10^{16}$ cm^{-3}, for defect levels with energies 270/605/880 meV (circles, squares, stars) above valence band. With capture cross sections $\sigma_{bt,n/p}=\sigma_{it,n/p}=10^{-14}$ cm^2 (open symbols), the power conversion efficiency increases only in the case of $E_{it}=270$ meV, by 0.4% absolute when all defects are concentrated at the GB ($N_{it}=4\times10^{12}$ cm^{-2}). Taking $\sigma_{bt,n/p}=\sigma_{it,n/p}=10^{-13}$ cm^2 (closed symbols) results in an increase in the efficiency of around 3% absolute for all three defect energies. This result with highly recombination active defects is consistent with the scaling law of Ref. 32. This law states that at a given number of recombination centers the concentration of these defects in well separated cell areas (here, the GBs) is always a more favorable situation compared to a spatially homogeneous distribution of these defects. However, a benefit of defects concentrated at the GB instead of distributed in the bulk is guaranteed only in cases where the defects have sufficiently strong recombination activity. When defects are less active, as seen in Fig. 7(a) from the curves where $\sigma_{n/p}=10^{-14}$ cm^{-2}, the shift of the defects from the bulk to the GB slightly rise the device efficiency only when the defect energy is lower than midgap (open circles), and harms the device performance if the defects lie near/above midgap (open squares and open stars).

E. Collection of carriers along grain boundaries

The enhancement of carrier collection along inverted grain boundaries has been discussed as one possible advantage of polycrystalline semiconductors with respect to their monocrystalline counterparts. From the experimental evidence it appears that type inversion applies rather to CdTe solar cells[4,5] whereas in CIGS (Refs. 7–9, 12, 16, and 17) the band bending around the GB is relatively small. Hence, the following calculations aim more at a general understanding of carrier collection along GBs than to the real situation in CIGS.

As we have already seen in Fig. 4, an improvement of carrier collection by inverted GBs is overcompensated by the increase in GB recombination when taking a high performance CIGS bulk as a starting point. Therefore, we explore

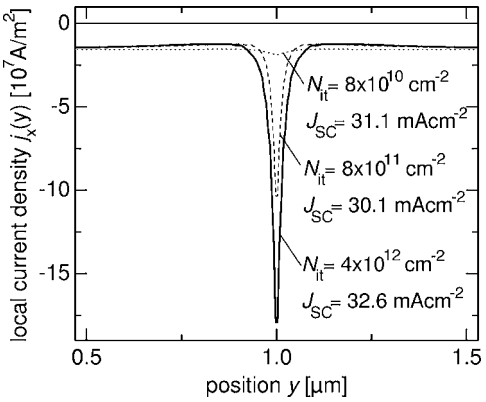

FIG. 9. Profiles of the vertical component of the local current density j_x calculated at a depth of 100 nm, i.e., close to the cell junction. The profiles are calculated under illumination, short circuit conditions, for grain boundary (GB) defect densities of $N_{it}=8\times10^{10}/8\times10^{11}/4\times10^{12}$ cm^{-2}.

now the situation of a rather mediocre bulk material. The assumed bulk defects have an energy 605 meV above the valence band edge, a concentration $N_{bt}=2\times10^{15}$ cm^{-3}, and capture cross sections $\sigma_{bt,n/p}=10^{-14}$ cm^2, corresponding to a bulk diffusion length $L_D\approx1.1$ μm. The reference computation for a GB trap density $N_{it}=0$ yields a photovoltaic performance of $\eta\approx16\%$ and $J_{SC}\approx31$ mA cm^{-2}, as shown in Fig. 8. Consistently, these values are somewhat lower than those obtained in Fig. 4 where smaller $\sigma_{bt,n/p}=10^{-15}$ cm^2 were taken. The introduction of GB defects at energy $E_{it}=E_V+880$ meV with capture cross sections $\sigma_{it,n/p}=10^{-14}/10^{-15}/10^{-16}$ cm^2 leads to an enhancement of J_{SC} up to 32.6 mA cm^{-2} at $N_{it}=4\times10^{12}$ cm^{-2}. However, an overall improvement of the efficiency η is not observed, as the gains in J_{SC} are overcompensated by the losses in V_{OC}. The trap density $N_{it}=4\times10^{12}$ cm^{-2} corresponds to an addition of 2×10^{16} cm^{-3} to the total defect concentration. In the case of low capture cross section $\sigma_{it,n/p}=10^{-16}$ cm^2 (circles in Fig. 8), this adds roughly only 10% to the recombination in the grain interior with $N_{bt}=2\times10^{15}$ cm^{-3} and $\sigma_{bt,n/p}=10^{-14}$ cm^2. Therefore, we conclude that losses in V_{OC} are a combination of the additional GB recombination *and* a higher recombination through bulk defects in the space-charge region surrounding the GB. Even considering cases where the carrier mobilities are an order of magnitude lower (results not shown here) and the different combinations of bulk and GB capture cross sections used above, we have not identified a situation where the introduction of an inverted GB in the way described here leads to an enhanced efficiency of the solar cell.

The improvement in J_{SC} seen in Fig. 8(b) does only weakly depend on the chosen capture cross section, indicating that carrier collection is effectively enhanced by the GB provided *sufficient type* inversion is achieved. Interestingly, for intermediate concentrations and the larger capture cross sections, the J_{SC} data exhibit a minimum, pointing to a non-negligible effect of GB recombination on carrier collection. To shed some light into the enhancement of J_{SC} with increasing N_{it}, we calculate spatial profiles of the perpendicular current density component j_x close to the heterojunction ($x=100$ nm). These profiles (shown in Fig. 9) correspond to the simulations of Fig. 8(b) belonging to the curve with $\sigma_{it,n/p}=10^{-15}$ cm^2 for $N_{it}=8\times10^{10}$ (dotted)/8×10^{11} (dashed)/4×10^{12} (continuous) cm^{-2}. For clarity, the curves are displayed in the interval $0.5\ \mu m<y<1.5\ \mu m$. At $N_{it}=8\times10^{11}$ cm^{-2} (dashed curve), the cell operates at the onset of type inversion at the GB. All three profiles reflect that with increasing band bending (higher N_{it}) the current density becomes increasingly concentrated at the GB. However, this *current crowding* effect leads to higher J_{SC} values only if the recombination probability around the GB is lower than in the bulk. Such a condition is only achieved when sufficient-type inversion in the surroundings of the GB is attained. This explains that the dashed curve in Fig. 9 yields the lowest J_{SC} value, since at the onset of inversion, the carrier concentrations at the GB are nearly equal, yielding maximum recombination rates. The case with $N_{it}=4\times10^{12}$ cm^{-2} (continuous curve in Fig. 9) has a much stronger inverted population around the GB, which result in an improved J_{SC}.

IV. EFFECT OF THE INTERNAL BAND OFFSET

A. Excess barrier height

It has been suggested in the past that one important ingredient for the high performance of polycrystalline CIGS thin-film solar cells stems from an internal valence band offset ΔE_V at the GBs (sometimes also referred to as a neutral barrier) resulting from a slightly Cu-poor composition of the region adjacent to the GB.[13–15] The effect of this internal offset at the GBs could be of similar importance as it is at the surface of the absorber,[33] whereas, there is ample experimental evidence for the Cu-poor surface layer[34,35] and its beneficial consequences for the performance of CIGS solar cells as long as the overall film composition is Cu-poor,[36] the question whether or not such a Cu-poor layer is a general positive feature of GBs in CIGS is still under discussion.[37–40]

The present study concentrates on investigating the effect of such an internal band offset and on finding the conditions that have to be fulfilled if the Cu-poor layer should have a decisive beneficial effect on the performance of polycrystalline CIGS solar cells. Figure 10 shows the band diagram of a GB surrounded by a Cu-poor layer that has a valence band offset ΔE_V toward the CIGS bulk. In such a situation, the hole barrier at the GB is enhanced leading to an effective barrier $\Phi_b^*=\Phi_b+\Delta E_V$. Note that only the part Φ_b results from the interface charges Q_{it} whereas the internal valence band offset ΔE_V leads to an additional contribution that is sometimes referred to as *neutral barrier*.[14,17]

This additional barrier prevents holes from the grain interior to reach the location of the GB. As long as the GB is parallel to the direction of carrier transport, we can assume that the band offset does not affect carrier transport in the direction to the collecting junction. Then, the effect of the internal band offset is the reduction of carrier recombination. In the following, we model recombination at the GB with the help of a reduced effective hole capture cross section $\sigma_{it,p}^{eff}$, which in the Appendix is shown to obey

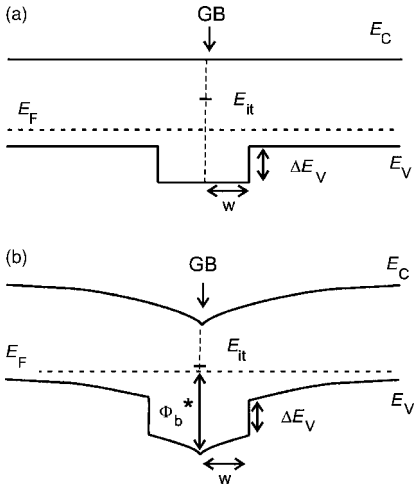

FIG. 10. Band diagram across an uncharged, flatband GB displaying an internal valence band offset of ΔE_V at the location of the grain boundary (a), and across a charged GB (b) with a band bending qV_b. The energy of the defect level at the GB is E_{it}.

$$\sigma_{it,p}^{eff} = \sigma_{it,p} \exp(-\Delta E_V/kT), \quad (7)$$

where kT denotes the thermal energy. Note that according to Eq. (7), one order of magnitude in the ratio $r_\sigma = \sigma_{it,p}^{eff}/\sigma_{it,p}$ corresponds almost exactly to an increment of the band offset ΔE_V by 60 meV at room temperature.

Let us first assume a high GB defect concentration ($N_{it} = 4\times10^{12}$ cm^{-2}), serving as limiting cases for maximum GB recombination activity, to gain a general overview on the effect of the internal band offset. Figure 11 compares the conversion efficiency η, short circuit current densities J_{SC}, and open circuit voltages V_{OC} as a function of the ratio r_σ, assuming $\sigma_{it,p} = \sigma_{it,n} = 10^{-15}$ cm^2. These simulations use bulk defect densities $N_{bt} = 2\times10^{15}$ cm^{-3}, and bulk capture cross sections $\sigma_{bt,n/p} = 10^{-15}$ cm^2. The defect energies are assumed equal in the bulk and at the GB, being $E_{it} = E_{bt} = E_t$ = 270 meV (circles)/605 meV (squares)/880 meV (diamonds). All energy values are taken relative to the valence band maximum in the grain.

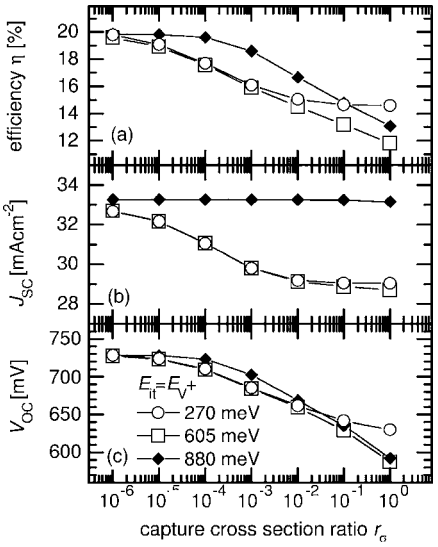

FIG. 11. Simulated efficiency η, short circuit current density J_{SC}, and open circuit voltage V_{OC} as a function of the ratio r_σ between effective hole and electron capture cross sections at the GB. Note that one order of magnitude in r_σ corresponds to an increment of the band offset ΔE_V by 60 meV. The defect density at the grain boundary is 4×10^{12} cm^{-2}.

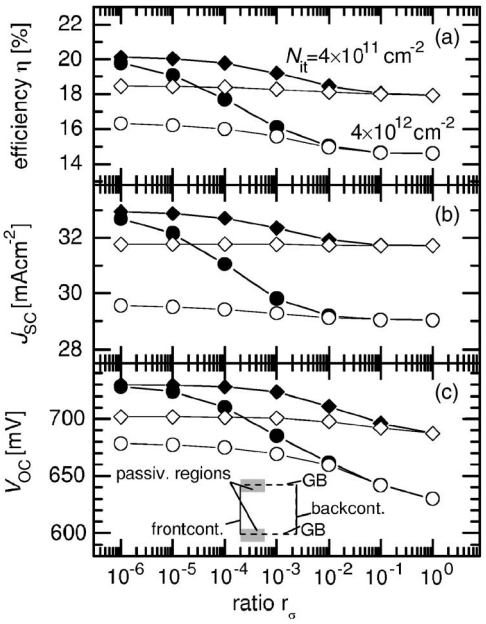

FIG. 12. Simulated efficiency η, short circuit current density J_{SC}, and open circuit voltage V_{OC} as a function of the ratio r_σ between effective hole and electron capture cross sections at the GB, for increasing grain boundary defect densities N_{it}. The defect energy is 270 meV above the valence band edge for bulk as well as for grain boundary defects. Open symbols stand for the case where the internal valence band offset extends along the hole length of the GB. Full symbols correspond to the situation where only the first third (0.66 μm) of the GB is passivated by the band offset as shown in the inset.

As shown in Fig. 11, decreasing values of the cross section ratio r_σ improve η, independently of E_{it}. Comparing the efficiency values at the extreme values of r_σ, η increases between 5% and 8% absolute (depending on the defect energy) when r_σ is reduced from 10° (equal capture cross sections, no GB band offset) to 10^{-6}, corresponding to a band offset of $\Delta E_V = 360$ meV. Although V_{OC} increases with decreasing r_σ independently of E_{it}, the short circuit current density shown in Fig. 11(b) drastically changes its behavior when E_{it} lies above midgap. Indeed, the simulations with $E_{it} = E_V + 880$ meV show a high $J_{SC} = 33$ mA cm^{-2} already at $r_\sigma = 10°$, with no influence of r_σ. This feature explains that the efficiency shown in Fig. 11(a) tends to be higher for the defect above midgap than for defects near or below midgap (squares, circles). This effect is explained by the phenomenon of improved carrier collection by inverted GB, guaranteed by the high defect density $N_{it} = 4\times10^{12}$ cm^{-2}.

In the next step, we deepen our analysis for the case of a rather shallow defect level in combination with band offsets, and intermediate defect densities. Figure 12 shows the output parameters as a function of r_σ, obtained for $E_{it} = E_V + 270$ meV and $N_{it} = 4\times10^{11}$ and 4×10^{12} cm^{-2}. The data points with $N_{it} = 4\times10^{12}$ cm^{-2} (open circles) are the same as in Fig. 11 (open circles). We see that at the lowest ratio $r_\sigma = 10^{-6}$, corresponding to $\Delta E_V = 360$ meV, all effects of GB recombination are eclipsed. Figure 12 shows that high efficiencies around 20% are possible for $N_{it} < 2\times10^{12}$ cm^{-2}, and ratios $r_\sigma \leq 10^{-5}$, i.e., band offsets $\Delta E_V \geq 300$ meV.

Additionally, Fig. 12 shows the calculated parameters (full symbols) under the assumption that the GB is passivated only to one-third of its length toward the front surface by the internal band offset as sketched by the inset in Fig. 12(c). Such an assumption is reasonable for two reasons. First, there is ample evidence that the Cu-poor region providing the internal valence band offset is present at the surface of the absorber.[34–36] It is therefore reasonable to conclude that a Cu-poor region at the GBs is more likely to be present toward the surface of the absorber than toward the back contact. Second, measurements of the majority-carrier transport properties of CIGS films in coplanar geometry, i.e., perpendicular to many GBs, exhibit activation energies in a range between 60 and 120 meV,[41] i.e., much smaller than an effective internal band offset. Therefore, the extra barrier cannot be present along the *full* length of *all* grains in the CIGS films. Rather, it might be present at some GBs and/or only for a part of the GB length.

A good passivation of GBs for the first 0.66 μm should be a relatively effective situation because at least recombination in the space charge region is reduced. This is reflected in the fact that V_{OC} moderately increases with decreasing r_σ (increasing ΔE_V) for the partially passivated GBs in Fig. 12(c). However, J_{SC} remains essentially unaffected by the increase in the internal barrier [Fig. 12(b)] resulting eventually in rather moderate improvements of the efficiency [Fig. 12(a)]. We conclude from this result that not only a high barrier height of at least 300 meV but also an almost homogeneous presence of the Cu-poor layer around the GBs along their entire length is required to virtually eclipse their deleterious impact on the device performance.

B. Influence of the barrier width

It is evident that a mere interface reconstruction is not sufficient to provide a sufficient interface passivation because holes may penetrate the extra barrier by quantum-mechanical tunneling. Therefore, only a sufficiently thick high band gap layers will prevent holes from tunneling into the interface states at the GBs. In the following, we investigate the tunneling effect considering a rectangular energy barrier with an energy height ΔE_V around the GB. The probability P_{Tun} to penetrate such a barrier is found in the WKB expression[42]

$$P_{\mathrm{Tun}} = \exp\left(\frac{-2w(2m^*\Delta E_V)^{1/2}}{\hbar}\right), \tag{8}$$

where w is the width of the barrier, i.e., the width of the Cu-poor wide-gap region on either side of the GB (cf. Fig. 10). The quantity $\hbar$ is Planck's constant and m^* denotes the effective mass of the hole in the Cu-poor interface layer (assumed to be 0.7 times the free electron mass m_e according to Ref. 43). Figure 13 displays the tunneling probability P_{Tun} (dotted lines) and the sum $P=P_{\mathrm{Tun}}+P_{\mathrm{TE}}$ (solid lines) that corresponds to the probability that a hole from the bulk of the grain arrives at the GB either by tunneling or by thermionic emission with the probability $P_{\mathrm{TE}}=\exp(-\Delta E_V/kT)$ (dashed lines in Fig. 13). As can be seen from Fig. 13, a barrier width $w>3$ nm is needed to reduce the tunneling probability to negligible values and, in consequence, the probability P to the thermionic-emission values given by Eq. (7). Note here that the transmission probability enters into our numerical simulations via the capture cross section ratio $r_\sigma=P$. Therefore, all results in Figs. 11 and 12 account either for a specific valence band offset together with a sufficient thickness $w\geq 3$ nm or for a given combination of $w\leq 3$ nm and ΔE_V where the resulting r_σ must be extracted from Fig. 12. Thus, we conclude that an almost perfect passivation of the GBs resulting from $r_\sigma\leq 10^{-5}$ in Figs. 10 and 11 not only requires a considerable band offset $\Delta E_V\geq 300$ meV but also a significant width $w\geq 3$ nm of the Cu-poor region on either side of the GB.

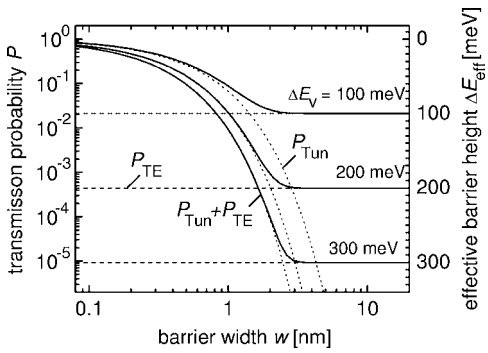

FIG. 13. Tunneling probability P_{Tun} (dotted lines), thermionic-emission probability P_{TE} (dashed lines) and combined probability $P=P_{\mathrm{Tun}}+P_{\mathrm{TE}}$ for carriers trespassing an energy barrier of width w and height $\Delta E_V=100/200/300$ meV. Roughly, beyond a barrier width $w>3$ nm, tunneling becomes negligible, remaining thermionic emission as the only transmission mechanism. The right axis indicates the effective barrier height ΔE_{eff} (see Sec. VG for details).

At this point, it is important to note that the considerations above are also valid for the passivation effect of the Cu-poor layer at *the surface* of CIGS films. This layer has a thickness that varies between 5 and 60 nm depending on the overall film composition.[44] Hence, tunneling could reduce the passivation effect of this surface layer in case of CIGS films that come very close to a stoichiometrical composition. Ensuring a sufficient thickness of the Cu-poor surface layer seems therefore of importance for high-efficiency CIGS solar cells. We argue that the last (Cu-free) deposition stage of the three-stage deposition process[45] for highest efficiency CIGS solar cells plays an important role in this context.

V. HORIZONTAL GRAIN BOUNDARIES

Grains in high-efficiency CIGS absorbers are preferentially columnar making the vertical GB model the most important one. However, GBs parallel to the cell's surface are present to a certain amount in all CIGS solar cells. This section investigates the impact of such horizontal GBs on the cell performance, according to the geometry sketched in Fig. 1, where the GB is placed at a depth $x=1$ μm. Here, we are particularly interested in the effect of the hole barrier, since it introduces an additional physical effect compared to the situation of the vertical GB: the action as an obstacle to *carrier transport*.

The effect of potential barriers on majority-carrier transport is usually modeled by lowering the carrier concentration

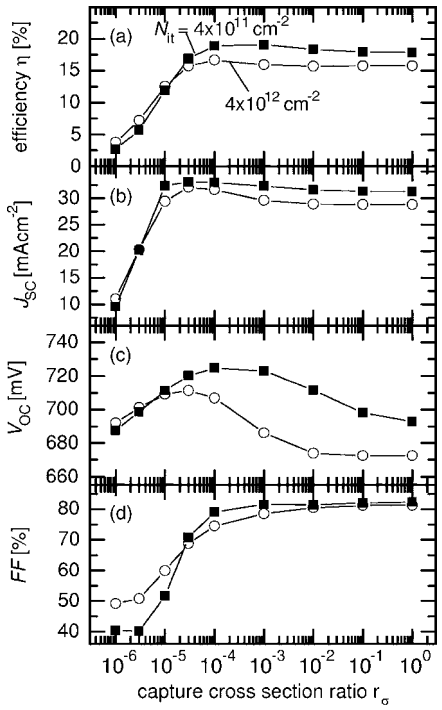

FIG. 14. Simulated solar cell parameters as a function of the ratio r_σ between effective hole and electron capture cross sections at the GB, for a cell with a horizontal GB located at the middle of the absorber. Note that no vertical GBs are present in these calculations. The curves are calculated for GB defect densities $N_{it}=4\times10^{11}/4\times10^{12}$ cm^{-2} (squares/circles). The defect energy is 270 meV above the valence band edge for bulk as well as for GB defects. The introduction of a hole barrier to the horizontal GB is beneficial only up to about $r_\sigma=10^{-3}-10^{-4}$. Below this range, the fill factor (FF) falls rapidly, followed by additional drops in J_{SC} and V_{OC}, with the expected drop of cell efficiency η.

within the barrier by the factor $\exp(-\Delta E_V/kT)$, or by keeping the carrier concentration constant and reducing the mobility by the same factor.[46] Here, we follow the latter strategy by assuming an effective hole mobility given by

$$\mu_p^{\text{eff}} = \mu_p \ \exp(-\Delta E_V/kT) = \mu_p r_\sigma \tag{9}$$

in the surroundings (±20 nm) of the GB.

The calculated solar cell output parameters as a function of r_σ are shown in Fig. 14. The curves are calculated for two GB defect densities N_{it} that differ by one order of magnitude, 4×10^{11} cm^{-2} (squares), and 4×10^{12} cm^{-2} (circles). For bulk and GB defects, a defect energy of 270 meV above the valence band edge and equal electron and hole capture cross sections $\sigma_{bt,n/p}=\sigma_{it,n/p}=10^{-15}$ cm^2 are assumed. Note that *no vertical* GB is assumed in the following calculations. As seen in the efficiency η [Fig. 14(a)], the introduction of a hole barrier to the horizontal GB is beneficial only up to $r_\sigma=10^{-3}-10^{-4}$, depending on N_{it} ($\Delta E_V=180-240$ meV). In this regime, the hole barrier acts similarly to the case of the vertical GB described previously, i.e., by reducing the recombination probability for holes. The overall efficiency improvement in this regime is due to an enhancement of the open circuit voltage [Fig. 14(c)]. At r_σ below 10^{-4}, the barrier hinders carrier transport and, therefore, strongly reduces the short circuit current density J_{SC}, the fill factor (FF), and consequently, the cell efficiency η. Especially, the fill factor FF shown in Fig. 14(d) monotonically decreases with decreasing r_σ. By comparing the values at the extremes of the r_σ axis, we notice that at $r_\sigma=10^{-6}$, J_{SC} and FF drop to about 1/3 and 1/2 of their values at $r_\sigma=10°$, respectively.

The results shown in Fig. 14 demonstrate that cell regions with horizontal GBs with a hole barrier that is wide and high enough to prevent recombination implies that hole transport across the same barrier becomes almost impossible. Especially for values $\Delta E_V>240$ meV where the reduction of carrier recombination becomes significant (cf. Figs. 11 and 12), an additional horizontal GB virtually eclipses the (local) short circuit current that would originate from light absorption in the front part of the grain.

VI. SUMMARY

The present paper investigates GB effects on the performance of CIGS solar cells, studying the effects of defect densities, energy levels and capture cross sections, grain size, and GB orientation (vertical and horizontal to the cell's surface). Our results show that the introduction of GB defects results in an overall efficiency loss from 20% to below 12%, making proper passivation of GBs a primary requirement for high efficiency. In order to reach $\eta=19\%$ with electron and hole capture cross sections of 10^{-15} cm^{-2} at vertical GBs, our results predict that low defect densities of $N_{it}=10^{11}$ cm^{-2} for a grain size of $g=0.5$ μm, and $N_{it}=2\times10^{11}$ cm^{-2} for $g=2$ μm are required. Such low defect densities yield negligible GB barrier heights. In order to reproduce the experimentally found GB barrier heights of 100 meV reported in the literature, our calculations require GB defect densities of 2×10^{12} cm^{-2}, considering a defect level at 270 meV above valence band edge. In such a situation, efficiencies of $\eta=19\%$ would require an electron capture cross section of 10^{-18} cm^2 (at the vertical GB).

Highly concentrated defects placed in the upper half of the band gap yield inverted GBs. Such inverted GBs improve the collection of photogenerated carriers in the cell, enhancing the short current density J_{SC}. However, η is not improved because this effect is counterbalanced by losses in V_{OC} associated with the required high defect concentration. Only when comparing monocrystalline and polycrystalline CIGS with the same *overall* number of defects we observe that redistributing these defects toward the GBs may improve the device performance especially for high defect concentrations and/or high defect capture cross sections. However, efficiencies η in excess of 16% are hardly compatible with a significant concentration of defects close to the conduction band and with inverted GBs.

We further simulate cells featuring a band offset in the valence band at the GB, a *hole barrier*, as a possible efficient passivation mechanism working at the GBs.[13,14] Barriers at least 300 meV high would effectively reduce recombination at the GB provided the barrier is present along the entire GB. Additionally, a minimum thickness of 3 nm is needed to prevent quantum-mechanical tunneling of carriers into the GB. However, barriers that fulfill these requirements for width and height are no longer beneficial when associated with horizontal GBs, where they act as obstacle for hole transport across the GBs. Thus, the hole barrier may play an

important role in CIGS films by passivating some, possibly the most recombination active, GBs. However, this barrier cannot be a general feature of *all* GBs in high-efficiency CIGS absorbers. The generally benign character of GBs must also embrace beneficial crystallographic GB structures[11,12] and defect chemical passivation of GB defects[18–21] in order to keep the defect density low.

ACKNOWLEDGMENTS

The authors are grateful to T. Kirchartz and J. H. Werner for collaboration and discussions. We also acknowledge M. Troviano (UNC) and B. Pieters (FZJ) for a critical reading of this manuscript.

APPENDIX: DERIVATION OF EFFECTIVE CAPTURE CROSS SECTIONS

Here, we obtain Eq. (7) considering the band diagram shown in Fig. 10(a), although the resulting expression is perfectly valid also for a charged grain boundary as in Fig. 10(b). By using the expression for the SRH recombination rate evaluated at the location of the GB, we demonstrate that the incorporation of a valence band offset ΔE_V at the GB alters the equation only by the hole capture cross section, which must be replaced by the effective capture cross section $\sigma_{\mathrm{it},p}^{\mathrm{eff}}$ given by Eq. (7). The recombination rate given by Eq. (3), depends on the electron and hole concentrations at the GB, given by $n_{\mathrm{it}}=N_C \exp[(E_{Fn}-E_C)/kT]$, $p_{\mathrm{it}}=N_V \exp[(E_V-E_{Fp})/kT]$, where E_{Fn} and E_{Fp} are the electron and hole quasi-Fermi energy levels, respectively. When a valence band offset ΔE_V is added, Eq. (3) must be rewritten using the following replacements:

$$p_{\mathrm{it}} \rightarrow p_{\mathrm{it}} \exp(-\Delta E_V/kT),$$

$$p_{1,\mathrm{it}} \rightarrow p_{1,\mathrm{it}} \exp(-\Delta E_V/kT). \tag{A1}$$

By performing these replacements, and considering that under solar cell operation n_i^2 is negligible, the recombination rate is given by

$$R_{\mathrm{it}} = \frac{N_{\mathrm{it}} v_{\mathrm{th}} n_{\mathrm{it}} p_{\mathrm{it}}}{\sigma_{\mathrm{it},p}^{-1} \exp(\Delta E_V/kT)(n_{\mathrm{it}}+n_{1,\mathrm{it}}) + \sigma_{\mathrm{it},n}^{-1}(p_{\mathrm{it}}+p_{1,\mathrm{it}})}. \tag{A2}$$

This expression indicates that when adding a valence band offset, R_{it} may be calculated as if there where no offset, but considering a hole effective capture cross section given by

$$\sigma_{\mathrm{it},p}^{\mathrm{eff}} = \sigma_{\mathrm{it},p} \exp(-\Delta E_V/kT). \tag{A3}$$

Since the recombination rate analyzed here is at the location of the GB, this expression is also valid for charged GBs with a band bending, as shown in Fig. 10(b).

[1] K. Ramanathan, M. A. Contreras, C. L. Perkins, S. Asher, F. S. Hasoon, J. Keane, D. Young, M. Romero, W. Metzger, R. Noufi, J. Ward, and A. Duda, Prog. Photovoltaics **11**, 225 (2003).
[2] P. Jackson, R. Würz, U. Rau, J. Mattheis, M. Kurth, T. Schlötzer, G. Bilger, and J.-H. Werner, Prog. Photovoltaics **15**, 507 (2007).
[3] Active area efficiency of a $CuInSe_2$ cell reported by C. H. Champness, H. Du, and I. Shih, Proceedings of the 29th IEEE Conference (IEEE, Piscataway, New York, 2002), p. 732. We notice that this cell uses a simple, unoptimized front contact (strongly suffering from series resistance), and no antireflection coating.
[4] I. Visoly-Fisher, S. R. Cohen, A. Ruzin, and D. Cahen, Adv. Mater. (Weinheim, Ger.) **16**, 879 (2004).
[5] I. Visoly-Fisher, S. R. Cohen, A. Ruzin, and D. Cahen, Adv. Funct. Mater. **16**, 649 (2006).
[6] S. Schuler, S. Nishiwaki, J. Beckmann, N. Rega, S. Brehme, S. Siebentritt, and M. Ch. Lux-Steiner, Proceedings of the 29th IEEE Photovoltaic Specialists Conference (IEEE, Piscataway, 2002), p. 504.
[7] S. Siebentritt and S. Schuler, J. Phys. Chem. Solids **64**, 1621 (2003).
[8] S. Sadewasser, Th. Glatzel, S. Schuler, S. Nishiwaki, R. Kaigawa, and M. Ch. Lux-Steiner, Thin Solid Films **431-432**, 257 (2003).
[9] T. Meyer, F. Engelhardt, J. Parisi, and U. Rau, J. Appl. Phys. **91**, 5093 (2002).
[10] M. J. Romero, K. Ramanathan, M. A. Contreras, M. M. Al-Jassim, R. Noufi, and P. Sheldon, Appl. Phys. Lett. **83**, 4770 (2003).
[11] N. Ott, G. Hanna, U. Rau, J. H. Werner, and H. P. Strunk, J. Phys.: Condens. Matter **16**, S85 (2004).
[12] G. Hanna, T. Glatzel, S. Sadewasser, N. Ott, H. P. Strunk, U. Rau, and J. H. Werner, Appl. Phys. A: Mater. Sci. Process. **81**, 1 (2006).
[13] C. Persson and A. Zunger, Phys. Rev. Lett. **91**, 266401 (2003).
[14] C. Persson and A. Zunger, Appl. Phys. Lett. **87**, 211904 (2005).
[15] M. J. Hetzer, Y. M. Strzhemechny, M. Gao, M. A. Contreras, A. Zunger, and L. J. Brillson, Appl. Phys. Lett. **86**, 162105 (2005).
[16] D. Azulay, O. Millo, I. Balberg, H.-W. Schock, I. Visoly-Fisher, and D. Cahen, Sol. Energy Mater. Sol. Cells **91**, 85 (2007).
[17] S. Siebentritt, S. Sadewasser, M. Wimmer, C. Leendertz, T. Eisenbarth, and M. Ch. Lux-Steiner, Phys. Rev. Lett. **97**, 146601 (2006).
[18] D. Cahen and R. Noufi, Appl. Phys. Lett. **54**, 558 (1989).
[19] U. Rau, D. Braunger, and H. W. Schock, Solid State Phenom. **67-68**, 409 (1999).
[20] L. Kronik, D. Cahen, and H. W. Schock, Adv. Math. **10**, 31 (1998).
[21] L. Kronik, U. Rau, J. F. Guillemoles, D. Braunger, H. W. Schock, and D. Cahen, Thin Solid Films **361-362**, 353 (2000).
[22] K. Taretto, U. Rau, and J. H. Werner, Thin Solid Films **480-481**, 8 (2005).
[23] M. Gloeckler, J. R. Sites, and W. K. Metzger, J. Appl. Phys. **98**, 113704 (2005).
[24] K. Taretto and U. Rau, in *Thin-Film Compound Semiconductor Photovoltaics*, edited by T. Gessert, K. Durose, C. Heske, S. Marsillac, and T. Wada, MRS Conference Proceedings No. 1012 (Materials Research Society, Pittsburgh, 2007), p. Y9-01.
[25] K. Orgassa, Ph.D. thesis, Universität Stuttgart, 2004.
[26] R. Hulstrom, R. Bird, and C. Riordan, Sol. Cells **15**, 365 (1985).
[27] F. Engelhardt, L. Bornemann, M. Köntges, Th. Meyer, J. Parisi, E. Pschorr-Schoberer, B. Hahn, W. Gebhardt, W. Riedl, and U. Rau, Prog. Photovoltaics **7**, 423 (1999).
[28] S. Selberherr, *Analysis and Simulation of Semiconductor Devices* (Springer, Vienna, 1984), p. 149.
[29] J. H. Werner, J. Mattheis, and U. Rau, Thin Solid Films **480-481**, 399 (2005).
[30] S. M. Sze, *Physics of Semiconductor Devices*, 2nd ed. (Wiley, New York, 1981), p. 35.
[31] For further information see: www.comsol.com.
[32] M. Schöfthaler, U. Rau, and J. H. Werner, J. Appl. Phys. **76**, 4168 (1994).
[33] T. Dullweber, G. Hanna, U. Rau, and H. W. Schock, Sol. Energy Mater. Sol. Cells **67**, 145 (2001).
[34] D. Schmid, M. Ruckh, and H. W. Schock, J. Appl. Phys. **73**, 2902 (1993).
[35] M. Morkel, L. Weinhardt, B. Lohmüller, C. Heske, E. Umbach, W. Riedl, S. Zweigart, and F. Karg, Appl. Phys. Lett. **79**, 4482 (2001).
[36] M. Turcu, O. Pakma, and U. Rau, Appl. Phys. Lett. **80**, 2598 (2002).
[37] M. J. Hetzer, Y. M. Strzhemechny, M. Gao, S. Goss, M. A. Contreras, A. Zunger, and L. J. Brillson, J. Vac. Sci. Technol. B **24**, 1739 (2006).
[38] M. J. Hetzer, Y. M. Strzhemechny, M. Gao, M. A. Contreras, A. Zunger, and L. J. Brillson, Appl. Phys. Lett. **86**, 162105 (2005).
[39] C. Lei, C. M. Li, A. Rockett, and I. M. Robertson, J. Appl. Phys. **101**, 024909 (2007).
[40] Y. Yan, R. Noufi, and M. M. Al-Jassim, Phys. Rev. Lett. **96**, 205501 (2006).
[41] A. Virtuani, E. Lotter, M. Powalla, U. Rau, J. H. Werner, and M. Acciarri, J. Appl. Phys. **99**, 014906 (2006).
[42] See, e.g., Eq. (46) on page 541 in Ref. 30.
[43] H. Neumann, Sol. Cells **16**, 317 (1986).
[44] I. M. Kötschau and H. W. Schock, J. Phys. Chem. Solids **64**, 1559 (2003).
[45] A. M. Gabor, J. R. Tuttle, D. S. Albin, M. A. Contreras, R. Noufi, and A. M. Hermann, Appl. Phys. Lett. **65**, 198 (1994).
[46] C. R. M. Grovenor, J. Phys. C **18**, 4079 (1985).